Clay Minerals (2026), **61**, 138–152
doi:10.1180/clm.2026.10032

Article

Identifying clay minerals and accessory phases by oxide composition using *MinMatch*

Laurence Noel Warr, Balu R. Thombare, Ritwick Sudheer Kumar and Georg H. Grathoff
Institute of Geography and Geology, University of Greifswald, Greifswald, Germany

Abstract

The accurate identification of clay minerals and associated phases remains challenging, particularly in fine-grained samples with complex assemblages. To assist in their identification, this study introduces *MinMatch*, a database and automated search program containing over 500 oxide compositions of clay minerals and their associated phases from soils, sediments and rocks. The program compares normalized oxide data with reference entries and ranks potential matches using Pearson correlation coefficients, supported by SiO_2:Al_2O_3 ratios and additional statistical and graphical parameters. Its performance is demonstrated using mineral oxide datasets from well-characterized samples of the 12th Reynolds Cup competition, derived from coarse- and fine-grained separates analysed using energy-dispersive X-ray spectroscopy combined with scanning and transmission electron microscopy. The results show that *MinMatch* consistently ranks compositionally equivalent minerals among the top matches and successfully discriminates between closely related varieties. The approach provides a rapid, quantitative and reproducible tool for clay mineral studies, complementing X-ray diffraction and other analytical methods.

Keywords: Clay minerals; EDX (EDS) analysis; electron microscopy; mineral identification; oxide chemistry; Reynolds Cup

(Received 17 December 2025; revised 9 March 2026; Accepted 23 March 2026)

The accurate identification and compositional characterization of clay minerals and associated phases are fundamental to a wide range of basic and applied scientific disciplines, including Earth sciences, soil science, chemistry, environmental studies and materials engineering (Bergaya & Lagaly, 2013; Biswas *et al.*, 2024). Clay minerals are typically fine-grained and frequently occur as complex intergrowths, posing significant challenges for identification, classification and eventual quantification. Conventional crystallographic and spectroscopic techniques, most notably X-ray diffraction (XRD) and Fourier-transform infrared (FTIR) spectroscopy, remain essential tools in clay mineral studies (Brindley & Brown, 1984; Moore & Reynolds, 1997; Madejová, 2003; Środoń, 2006). However, these methods can be limited by poor crystallinity, peak overlap and the presence of mixed-layer or amorphous phases. In such cases, micro-scale chemical compositional data provide important complementary information for reliable mineralogical characterization, particularly when diffraction or spectroscopic results are ambiguous or inconclusive.

Quantifying elemental abundances and oxide compositions provides further insight into the crystal-chemical characteristics of clay minerals. These data can be used to derive structural formulas, estimate layer charge and differentiate between dioctahedral and trioctahedral members of principal clay mineral groups, such as kaolinite-serpentine, illite, smectite and chlorite (Brindley & Brown, 1984; Newman & Brown, 1987; Brigatti, 2018; Garcia-Romero *et al.*, 2021). Compositional data are typically acquired using techniques such as energy-dispersive X-ray spectroscopy (EDX or EDS) combined with scanning or transmission electron microscopy (SEM/TEM), electron probe microanalysis (EPMA) or bulk analytical methods including X-ray fluorescence (XRF) and inductively coupled plasma optical emission spectroscopy (ICP-OES) or inductively coupled plasma mass spectrometry (ICP-MS).

For compositional data to be meaningful in mineral identification, a rigorous and well-controlled analytical methodology is required. This begins with careful sample preparation aimed at isolating pure mineral separates, although complete separation from intergrown or admixed phases is often difficult to achieve. Accurate determinations also require appropriate calibration procedures and the absence of mineral-specific measurement artifacts, such as electron beam damage incurred during microanalysis (Warr *et al.*, 2024). EPMA and EDX analyses are best conducted on well-polished, electrically conductive mounts, while ICP and XRF analyses use finely ground powders. As the oxygen concentration is difficult to measure accurately, the elemental data are often normalized to a specific number of oxygens to calculate oxide abundances or cation proportions, which are determined based on known molecular weights and stoichiometries (Droop, 1987; Deer *et al.*, 1992, 2013). For phyllosilicate clay minerals, the cations are then assigned to specific crystallographic sites, such as

Corresponding author: Laurence Noel Warr; Email: warr@uni-greifswald.de
Cite this article: Warr LN, Thombare BR, Sudheer Kumar R and Grathoff GH (2026) Identifying clay minerals and accessory phases by oxide composition using *MinMatch*. *Clay Minerals* **61**, 138–152. https://doi.org/10.1180/clm.2026.10032

© The Author(s), 2026. Published by Cambridge University Press on behalf of The Mineralogical Society of the United Kingdom and Ireland. This is an Open Access article, distributed under the terms of the Creative Commons Attribution licence (http://creativecommons.org/licenses/by/4.0), which permits unrestricted re-use, distribution and reproduction, provided the original article is properly cited.

tetrahedral or octahedral positions, based on established structural criteria (Newman & Brown, 1987). Additionally, diagnostic elemental ratios, such as Si:Al, Fe:Mg and K:Na, are commonly used to distinguish among mineral groups (Deer *et al.*, 1992, 2013; Stanley, 2020; Boraiy *et al.*, 2024). The total octahedral cation occupancy also helps determine whether a clay mineral is dioctahedral or trioctahedral. These compositional markers are particularly useful for identifying solid-solution trends and estimating layer charge in expandable clay minerals such as smectites and vermiculites (Vali *et al.*, 1993; Christidis *et al.*, 2023).

To support identification, calculated compositions are compared against established mineral standards. This can be achieved by consulting published compositional results or using digital databases and software tools. A search-match program has been proposed for the International Centre for Diffraction Data (ICDD) PDF-4 database, containing over 20,000 compositions (Fawcett *et al.*, 2018). However, such programs perform poorly for clay minerals with similar chemistry, and selecting an appropriate match can be challenging, because many compounds in the database are rare or not relevant to natural samples. Numerous software programs also exist for identifying minerals based on stoichiometry, although these are often limited either by database size or by specialization in particular mineral groups (Yavuz, 2003; Yavuz *et al.*, 2015; Siebach *et al.*, 2026). Another limitation of this approach is its reliance on assumptions regarding the number of anions or cations in the structure. Additionally, this process can be complicated by the presence of trace elements that are not part of the mineral structure, such as elevated concentrations of iron oxides from nanoparticles (Xia *et al.*, 2021; Biswas *et al.*, 2023; Sudheer Kumar *et al.*, 2026).

Another established approach for quantifying and mapping the composition of coarse-grained minerals is automated SEM-EDX mineral identification (Gottlieb *et al.*, 2000; Gu, 2003; Fandrich *et al.*, 2007). This method combines backscattered electron images and EDX analyses to match minerals in polished mounts to a reference database and to systematically map their spatial distribution. It has also been applied to sedimentary and clay-bearing materials (Pirrie *et al.*, 2013; Han *et al.*, 2022). However, automated SEM-EDX is primarily effective for larger grains and is generally less suitable for ultra-fine, clay-sized fractions, which are difficult to polish and require targeted manual analysis due to heterogeneous compositions and overlapping grains.

In this paper, a simple, purpose-built *MinMatch* database for clay minerals and associated phases is presented, based on oxide compositional data. The database currently contains over 500 reference mineral compositions, of which 373 represent well-constrained clay mineral compositions (reported in oxide weight %) from the literature, while the remaining entries correspond to accessory minerals. Many of the compositions were taken from standard reference volumes published by the Mineralogical Society of UK & Ireland, specifically Wilson (2013) for clay minerals and Deer *et al.* (1992, 2013; Fleet, 2003) for the accessory minerals. Additional compositions were selected from peer-reviewed research papers using the following criteria: (1) the analytical data were considered reliable, based on clearly described methods; (2) analyses were conducted on minerals of sufficient purity; and (3) compositional data were reported in oxide form. The program includes a search-and-match algorithm that employs the Pearson correlation coefficient for ranking potential minerals and offers additional statistical and visual means to evaluate compositional similarity. As an illustration of the program's application, this contribution reports on its testing using the well-characterized 12th Reynolds Cup samples from the 2024 competition, providing an unbiased assessment of its mineral identification capabilities.

Sample preparation and data acquisition

The *MinMatch.xls* spreadsheet program was used during participation in the Clay Minerals Society's 12th Reynolds Cup, where both SEM and TEM analyses were conducted in an open-competition setting. These samples were chosen because they provided a comprehensive collection of clay minerals and associated phases, making them ideal for testing the performance of the *MinMatch* program (Table 1). At that time, the James Hutton Institute in Aberdeen, Scotland (courtesy of S. Hillier), provided three well-characterized reference samples of known mineralogy; however, their contents were not disclosed to participants and were described as follows: (1) RC12-1, a kaolin; (2) RC12-2, a brown bentonite; and (3) RC12-3, an Old Red Sandstone. According to the information provided, the mineral powders were manually hand-ground prior to mixing to ensure homogeneity.

A portion (1 g) of each sample was dispersed in 1 L of double-distilled water and subjected to ultrasonic treatment at 50–60 Hz for 15 min. The >2 μm size fraction was then allowed to sediment according to Stokes' Law, and the <2 μm size fraction remaining in suspension was carefully decanted from the glass beaker and dried in an oven at 60°C to obtain the fine solid fraction. The remaining >2 μm size fraction was subsequently resuspended in 1 L of water, and the procedure was repeated until no significant quantity of the <2 μm size fraction could be separated. Once dried, both the <2 μm and >2 μm size fractions were homogenized manually using an agate mortar and pestle.

A small portion (~75 mg) of the <2 μm size fractions was added to 10 mL of ethanol in separate glass vials. After dispersion using an ultrasonic bath, a few drops of each suspension were deposited onto a holey carbon film supported on a specimen grid. To evaluate sample purity and dispersion quality, a second set of <1 μm size fractions was prepared by gravity settling.

The specimens were analysed using TEM-EDX following the methods of Warr *et al.* (2024). Data were acquired from ~1 μm^2 areas in parallel-beam TEM mode, with careful attention given to count times, beam-induced damage and calibration. Totals of 123, 40 and 81 particle analyses were obtained for RC12-1, RC12-2 and RC12-3, respectively. Measurement areas were chosen to target signals from individual minerals; however, due to the frequent occurrence of clay mineral aggregates, it was not always possible to ensure measurement purity, particularly where different clay minerals were stacked or intergrown. Overall, data acquisition required ~1 full day of TEM time per sample.

A small amount of the >2 μm size fraction was also added to 10 mL of ethanol in a small glass vial. Following mixing and sonication, a few drops of the coarse mineral suspension were pipetted onto a SEM sample stub lined with double-sided conductive carbon tape. The concentration of suspension was adjusted to obtain an even distribution of mineral grains with minimal overlap, while ensuring that each imaged area contained several tens of measurable particles. Prior to field-emission secondary electron imaging, samples were sputter-coated with a thin palladium layer to enhance surface conductivity and to minimize charging. SEM-EDX analyses were performed using a Zeiss Auriga FIB-SEM equipped with an X-MAX 80 mm^2 silicon drift detector. The elemental mapping function was applied, followed by analysis of the stored EDX data. In general, the fine-grained particles (<2 μm) were successfully removed during grain-size separation, except in RC12-2, where some fine material remained attached to larger grains.

https://doi.org/10.1180/clm.2026.10032 Published online by Cambridge University Press

Table 1. Mineral abundance of the three 12th Reynolds Cup mixtures provided by S. Hillier. Those identified in SEM (>2 μm) and TEM (<2 μm) studies are in bold.

	RC12–1 SEM	RC12–1 TEM	RC12–2 SEM	RC12–2 TEM	RC12–3 SEM	RC12–3 TEM
Clay minerals						
Kaolinite	**50.4**	**50.4**	**2.1**	**2.1**	**3.6**	**3.6**
Halloysite	**4.1**	**4.1**				
Mica (dioctahedral)	**1.8**	**1.8**	**1.2**	**1.2**	**0.1**	0.1
Illite-smectite (70%–30%)					**2.8**	**2.8**
Montmorillonite (Ca, Na)	**6.9**	**6.9**	**48.5**	**48.5**		
Nontronite			**15.9**	**15.9**		
Phlogopite			**1.0**	**1.0**		
Biotite	**3.1**	**3.1**	**1.9**	**1.9**	**1.1**	**1.1**
Chlorite (Mg)					**1.5**	**1.5**
Chlorite (Fe)					**2.3**	**2.3**
Score	5/5	5/5	6/6	6/6	6/6	5/6
Accessory minerals						
Quartz	**9.7**	**9.7**	**6.0**	**6.0**	**52.6**	**52.6**
Cristobalite			3.4	3.4		
Sanidine	**2.4**	**2.4**	**1.3**	**1.3**		
Microcline					**5.9**	**5.9**
Albite			**2.2**	**2.2**	**4.3**	**4.3**
Labradorite			**4.0**	**4.0**	**4.6**	**4.6**
Garnet					**2.4**	**2.4**
Epidote					0.8	0.8
Zircon					**1.1**	**1.1**
Calcite	**0.1**	0.1			**3.9**	**3.9**
Aragonite	2.0	2.0				
Dolomite					**1.3**	**1.3**
Ferroan Dol/Ank					**2.6**	**2.6**
Siderite	2.1	2.1			**2.0**	**2.0**
Goethite	**2.2**	**2.2**	2.2	2.2		
Hematite	1.8	1.8	Trace	Trace	**2.0**	2.0
Magnetite			1.0	**1.0**		
Apatite	**2.1**	2.1	**1.0**	**1.0**	0.1	0.1
Pyrite	**1.7**	1.7				
Rutile	**1.1**	**1.1**			**2.0**	**2.0**
Anatase	**2.1**	**2.1**			0.1	0.1
Halite					1.6	1.6
Baryte (Sr)					**1.1**	**1.1**
Heulandite/clinoptilolite			**1.9**	**1.9**		
Analcime			1.0	1.0		
Opaline silica	**6.4**	**6.4**				
Obsidian			6.0	6.0		
Bassanite			0.1	0.1		
Amphibole			0.1	0.1	Trace	Trace
Corundum					0.2	0.2
Ilmenite					0.1	0.1
Talc					Trace	Trace
Score	9/12	11/12	6/14	6/14	13/21	11/21

Ank = ankerite; Dol = dolomite.

Based on visual inspection of the secondary electron images and corresponding elemental maps, the EDX data were selectively processed for areas representing individual grains or monomineralic aggregates. Multiple regions were chosen to obtain representative spectra of sufficient intensity while minimizing interference from neighbouring grains. However, in practice, signals from adjacent grains could not always be avoided. Consequently, data collection proceeded in a stepwise manner, allowing unsatisfactory analyses to be promptly excluded from the dataset.

This methodology is described in detail in Podlech *et al.* (2021) and is summarized here. EDX mapping and secondary electron images were acquired at 10 kV and at a working distance of <5 mm, typically using magnifications between 448× and 656×. Mappings used a dwell time of 100 μs and total acquisition times of between 60 and 90 min. Data processing was performed using the *INCA* software (Oxford Instruments), which applied peak and background fittings, pulse pile-up, escape peak and atomic number (Z), absorption (A) and fluorescence (F) corrections. To avoid

https://doi.org/10.1180/clm.2026.10032 Published online by Cambridge University Press

reliance on oxygen measurements, the results were normalized to 100%, assuming all cations were present as oxides. The presence of other anions was assessed by examining chlorine and sulfur signals. Standardization of the elemental oxide concentrations was verified by measuring ASTIMEX silicate standards of similar oxide concentrations, with measurement accuracies reported by Podlech *et al.* (2021). A total of 8 maps and 197 mineral analyses were obtained for RC12-1, 6 maps and 126 analyses were obtained for RC12-2 and 5 maps and 203 analyses were obtained for RC12-3. SEM data acquisition required ∼1–2 days per sample, totalling ∼1 week of beam time.

All of the TEM and SEM compositional analyses obtained in this study are provided as Supplementary Material.

Database and using *MinMatch*

The database currently includes more than 370 clay mineral data files (Fig. 1a). These are grouped into 51 varieties of clay minerals, the most common being chlorite (not differentiated, n = 36), montmorillonite (n = 35), kaolinite (n = 26) and mixed-layered illite-smectite (n = 23). Other minerals represented by multiple compositions (n = 10–20) are dickite, illite, celadonite, nontronite, saponite, talc-smectite, chlorite-smectite and corrensite. All remaining species are represented by between one and nine individual compositions.

In addition to clay mineral species, a range of common accessory phases occurring in the clay-sized fraction of soils, sediments and rocks are included in the database (Fig. 1b). These currently comprise 124 compositions, derived largely from Deer *et al.* (1992) and associated mineral volumes of the Mineralogical Society of London. This part of the database contains numerous types of framework silicates (feldspars, n = 23; zeolites, n = 13; quartz, n = 1), chain silicates (amphiboles, n = 18; pyroxenes, n = 16) and ortho-, di- and ring silicates (e.g. garnet, n = 6; olivine, n = 4; epidote, n = 4; titanite, n = 3). A range of non-silicate minerals was also added, including oxides (corundum, ilmenite, rutile and spinel), carbonates (calcite, dolomite and siderite) and phosphates (e.g. apatite). Several amorphous glass phases are also included, which were initially absent during the Reynolds Cup testing of the *MinMatch* program reported in this study. The glasses span felsic (obsidian), intermediate (andesitic) and basic (basaltic) compositions.

MinMatch (available as Supplementary Material) is a *Windows OS*-based, *Excel*-based spreadsheet application (version LTSC Standard, *Office 2021*) with an integrated macro that performs a search-and-match procedure. Operation and database expansion require both macros, and the developer tab must be enabled. This version is incompatible with older *Excel* releases without modification, and additional adjustments may be necessary for *macOS*-based systems.

Each data file for a given mineral is organized vertically in separate columns, displaying the major oxide compositions in order of decreasing average abundance, calculated from the mean of all clay minerals in the database. The sequence is as follows:

$$SiO_2 > Al_2O_3 > MgO > Fe_2O_3 + FeO > K_2O > CaO > Na_2O > TiO_2 > Cr_2O_3 > P_2O_5 > (NH_4)_2O > Li_2O > NiO > MnO > SrO > P_2O_5 > V_2O_5 > CoO > BaO > ZnO$$

These oxides are listed in this order because they are more likely to produce curves that generally decrease in abundance from left to right (Fig. 2), thereby reducing the occurrence of strongly zigzagging curves that complicate visible pattern matching. If a different ordering is preferred, such as by atomic weight % (wt.%) or by molecular weight % of oxides, the rows in the data files can be easily re-sorted according to user preference. The oxide compositions are normalized to 100 wt.%, and hydrous components (OH^- or H_2O) are excluded to optimize the matching procedure.

In addition to oxide compositions, supplementary metadata are provided, including the literature source (first author and year), mineral location and, where available, geological information such as formation age and genetic origin (e.g. diagenetic, hydrothermal). Further descriptors, including the deposit type and the analytical method used to determine the composition, are also included. New minerals can be easily added to the *MinMatch* program database by modifying the macro formulas, as described within the program.

To use the *MinMatch* program, the first step is to input the 'unknown' raw oxide data into the appropriate column, marked 'raw data' (Fig. 2). The oxide data must have all hydrous components (H_2O, OH^-) removed and be normalized to 100 wt.% to match the format of the database. These corrections are necessary because the measured hydrous contents of clay minerals are often highly variable depending on drying conditions and analytical variability. Consequently, datasets can only be reliably correlated after this adjustment. Low concentrations of elements (commonly <0.1 wt.%), which may arise from impurities, can remain in the raw data input, as they do not significantly affect the matching results.

Once the data have been entered, the next step is to hit the 'RUN' button, which activates a macro that re-sorts the database based on the goodness of fit, as measured by the Pearson correlation coefficient (r). This statistic quantifies the linear relationship between the raw data and reference mineral compositions and is defined as per Equation 1:

$$r = \Sigma\left((x_i - \bar{x})\left(y_i - \bar{y}\right)\right) / \sqrt{\left(\Sigma(x_i - \bar{x})^2 \Sigma\left(y_i - \bar{y}\right)^2\right)} \quad (1)$$

where x_i and y_i are the oxide values of the raw and reference compositions, respectively, and $\bar{x}$ and $\bar{y}$ are their respective mean values. A value of $r = +1.0$ indicates a perfect positive correlation, $r = -1.0$ indicates a perfect negative correlation and $r = 0$ signifies the absence of any linear correlation.

In addition to the Pearson correlation coefficient (r), *MinMatch* also calculates the sum of the least squared differences (SDD) and the Euclidean distance. These parameters provide additional measures based on absolute compositional similarity. However, in practice, the Pearson correlation coefficient is considered sufficient for ranking the best matches, as it effectively captures both the linearity and the relative ratios of the oxide compositions.

As part of the optimization steps in the matching process, the SiO_2:Al_2O_3 ratio can be considered along with an examination of the raw curves and the reference data to facilitate visual comparison (Fig. 2). The best-fit dataset can then be selected based on a combined assessment of the Pearson correlation coefficient, SDD, Euclidean distance, SiO_2:Al_2O_3 ratio and the graphical information. In general, the closer the mineral match to multiple reference files of the same mineral types (e.g. illite-smectites), the more reliable the result. Such results can be easily copied into additional worksheets and arranged accordingly prior to any subsequent analyses.

https://doi.org/10.1180/clm.2026.10032 Published online by Cambridge University Press

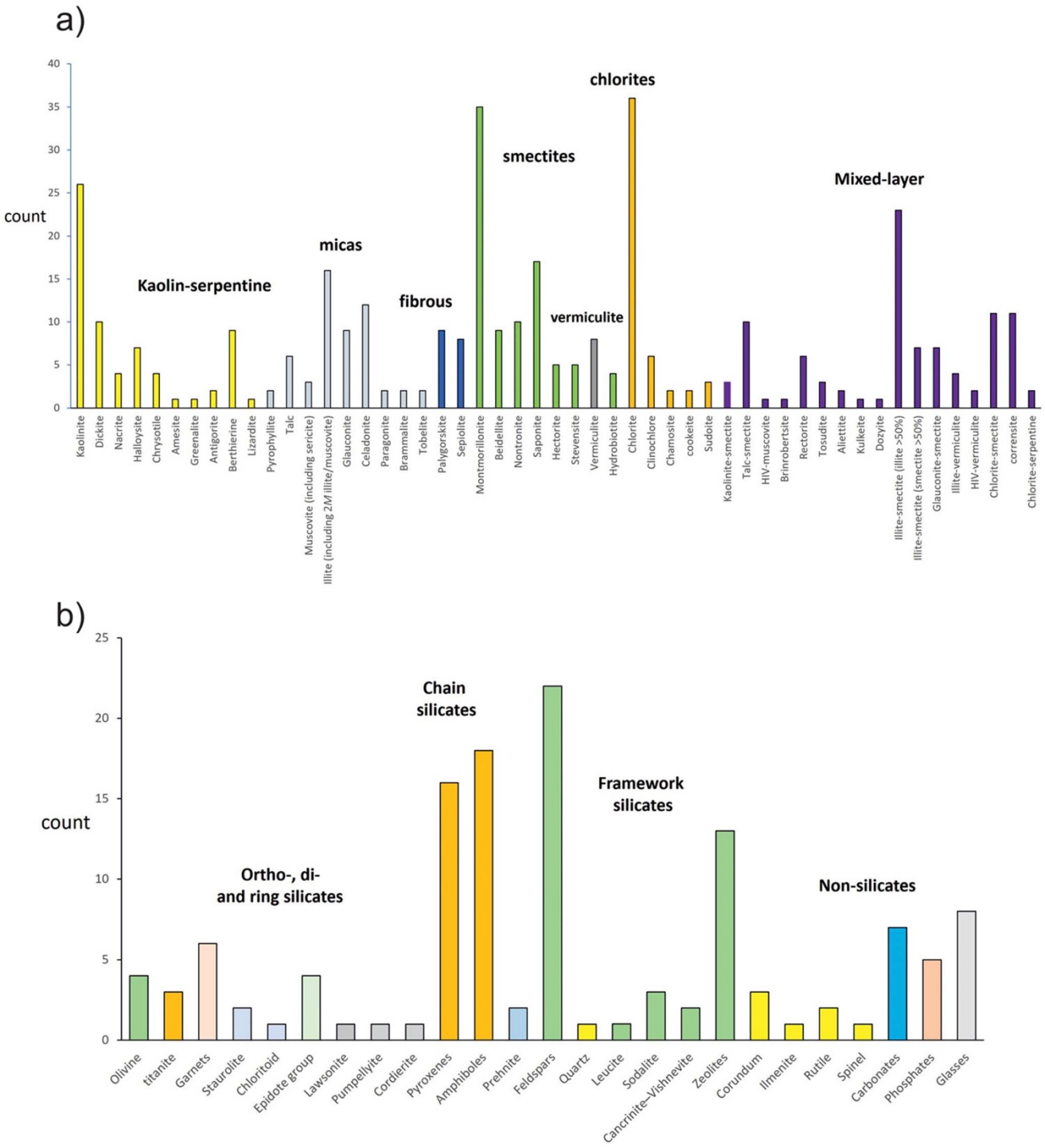


Figure 1. Mineral datasets included in the *MinMatch* program: (a) clay minerals and (b) accessory phases. Count = number of chemical compositions in the database. HIV = hydroxy-interlayered vermiculite.

Results

Based on the EDX compositional analyses, the clay minerals and other phyllosilicates within the sample mixtures were reliably identified without the need for XRD or other analytical methods (Table 1). In contrast, only ~60% of the accessory minerals were recognized using the same approach. A summary of these results is presented in the following subsections.

Composition analyses of clay minerals and other phyllosilicates

Due to the fine-grained nature of the clay minerals in the three samples, the TEM-EDX analyses of the <1 μm and <2 μm size fractions were preferred for compositional characterization, with the exception of some of the larger mica minerals, such as dioctahedral illite/muscovite, biotite and phlogopite, which were more accurately quantified using SEM-EDX (Table 2). In all three

https://doi.org/10.1180/clm.2026.10032 Published online by Cambridge University Press



Figure 2. User interface of the *MinMatch* program and illustration of the matching procedure. To use the program: (1) type in the mineral oxide raw data (normalized to 100%) in the field marked in orange; (2) hit the 'RUN' button to identify the best-fitting datasets sorted by Pearson correlation coefficient (*r*) values (labelled in red); (3) examine the SiO_2:Al_2O_3 ratios, sum of squared differences (SDD) and Euclidean distances as additional statistical criteria and (4) inspect the shapes of the matching graphs to optimize final selections (line graph = raw data, histogram = reference pattern). The example shown corresponds to the illite-smectite of the RC12-3 sample.

mixtures, the <1 μm size fractions generally contained a higher proportion of smectites and illite-smectites compared to the <2 μm size fractions, which were often more enriched in kaolinite and had a greater proportion of accessory minerals (e.g. quartz, iron oxides/oxyhydroxides and micas). Table 2 provides examples of how *MinMatch* can be used to characterize minerals in the test samples, and it illustrates how this information can be applied to optimize mineral recognition, with the support of the detailed EDX analyses provided as Supplementary Material. The best reference compositions fell within a Pearson correlation coefficient range of 0.9779–1.0000, and, based on repeat EDX analyses of the same mineral compositions, differences exceeding ±0.0002 were considered to be significant.

RC12-1

Thin, hexagonal-shaped crystals indicative of kaolinite were abundant in this sample, along with occasional halloysite nanotubes (Fig. 3). The kaolinite produced characteristic EDX compositions, composed largely of SiO_2 and Al_2O_3, whereas the halloysite nanotubes were more difficult to analyse and exhibited slightly lower SiO_2 and Al_2O_3 contents, along with elevated concentrations of Fe_2O_3, MgO and CaO. The best *MinMatch* fit for these analyses was a mixed-layered kaolinite-montmorillonite (76%-24%), which probably reflects contamination from surrounding smectite minerals concentrated in the fine-grain-size fractions.

In addition to the kaolinite-group minerals, smaller quantities of a smectite were detected in the clay-sized fraction with a composition similar to that of the Tatatilla montmorillonite, which contains interlayered Ca and Na (Ross & Hendriks, 1945). An estimated average structural formula, based on a dioctahedral structure, for these compositional analyses is:

$$(Si_{3.88}Al_{0.12})(Al_{1.64}Fe_{0.12}Mg_{0.24})(Ca_{0.13}Mg_{0.04}Na_{0.02})O_{10}(OH_2)$$

with a total layer charge of –0.36 (tetrahedral charge –0.12, octahedral charge –0.24) per $O_{10}(OH_2)$ and dominated by Ca and Mg interlayered cations.

Other phyllosilicates detected in this mixture included a dioctahedral mica and biotite. SEM-EDX analyses (Table 2) indicate that their compositions are comparable to an illite/muscovite $2M_1$ from the Cameros Basin (Barrenechea *et al.*, 2000) and a biotite from the San Juan volcanic field of Colorado (Larsen *et al.*, 1937). Although the determination of the biotite composition is relatively old, it remains widely accepted and has been retained in standard reference textbooks for over 50 years (Deer *et al.*, 1992; Fleet, 2003). More recent biotite compositional datasets have not yet been incorporated into the *MinMatch* program.

RC12-2

The most abundant clay mineral present in the fine-grained fractions of the RC12-2 mixture was smectite, which occurred in two distinct compositions: (1) a Ca-montmorillonite and (2) an Fe-rich smectite. Based on TEM-EDX analyses (n = 19), the structural formula of the Ca-montmorillonite can be expressed as:

$$(Si_{3.95}Al_{0.05})(Al_{1.56}Fe_{0.15}Mg_{0.29})(Ca_{0.11}Mg_{0.04}Na_{0.04}K_{0.01})O_{10}(OH_2)$$

with a total layer charge of –0.34 (tetrahedral charge –0.05, octahedral charge –0.29) per $O_{10}(OH_2)$ and dominated by Ca, Mg and Na interlayered cations.

https://doi.org/10.1180/clm.2026.10032 Published online by Cambridge University Press

Table 2. Best-selected clay mineral compositions determined by SEM-EDX or TEM-EDX and their corresponding best match (bold) from the *MinMatch* database. All oxide compositions were normalized to 100% ± 0.5% to ensure internal consistency among datasets.

Mineral	Method	*n*	*r*	SiO_2	TiO_2	Al_2O_3	Fe_2O_3	MnO	MgO	CaO	Na_2O	K_2O
RC12–1												
RC12–1 Kln	TEM	48	–	53.72	0.22	44.46	0.76	0.04	0.34	0.23	0.02	0.20
Athabasca Kln[a]	**EMPA**	**2**	**1.0000**	**54.37**	**0.00**	**44.52**	**0.39**	**0.01**	**0.28**	**0.09**	**0.12**	**0.20**
RC12–1 Hly	TEM	1	–	57.44	0.06	38.72	1.27	0.05	1.26	1.20	0.00	0.02
Kln-Mnt (76%–24%)[b]	**WC+AAS**	**1**	**0.9996**	**57.51**	**0.48**	**36.98**	**1.50**	**0.00**	**1.27**	**0.94**	**0.53**	**0.79**
RC12–1 di-mica	SEM	7	–	48.66	0.24	37.72	1.27	0.00	0.42	0.06	1.20	10.42
Cameros Ilt/Ms $2M_1$[c]	**EMPA**	**1**	**0.9999**	**48.55**	**0.22**	**38.38**	**1.42**	**0.00**	**0.75**	**0.00**	**0.74**	**9.95**
RC12–1 Mnt (Ca, Na)	TEM	1	–	66.02	0.19	25.46	2.66	0.07	3.28	2.10	0.18	0.04
Tatatilla Mnt[d]	**WC**	**1**	**0.9996**	**66.66**	**0.00**	**25.76**	**1.08**	**0.00**	**4.20**	**2.11**	**0.14**	**0.05**
RC12–1 Bt	SEM	29	–	46.11	1.87	14.11	17.00	0.51	11.87	0.14	0.64	7.74
Colorado Bt[e]	**WC**	**1**	**0.9944**	**40.60**	**4.43**	**13.59**	**18.66**	**0.14**	**13.22**	**1.70**	**0.73**	**6.79**
RC12–2												
RC12–2 Kln	TEM	3	–	54.01	1.11	41.03	2.26	0.15	0.71	0.54	0.17	0.06
Kemmlitzer Kln[f]	**TEM**	**22**	**0.9994**	**55.15**	**0.00**	**42.43**	**0.33**	**0.00**	**0.56**	**0.33**	**0.35**	**0.30**
RC12–2 di-mica	SEM	6	–	49.73	0.00	36.24	0.00	0.00	0.46	0.32	1.84	11.41
Athabasca Ilt $2M_1$[a]	**EMPA**	**4**	**0.9994**	**50.65**	**0.02**	**35.91**	**0.63**	**0.01**	**1.14**	**0.05**	**0.36**	**11.22**
RC12–2 Mnt	TEM	19	–	67.42	0.00	23.27	3.46	0.00	3.72	1.68	0.31	0.13
Wyoming Mnt[g]	**TEM**	**151**	**0.9996**	**66.23**	**0.00**	**23.78**	**4.40**	**0.00**	**3.60**	**0.60**	**1.10**	**0.30**
RC12–2 Non	TEM	23	–	60.94	0.00	16.40	17.04	1.07	1.93	1.87	0.40	0.12
Woburn Mnt[e]	**XRF**	**1**	**0.9958**	**62.51**	**0.46**	**16.84**	**13.38**	**0.00**	**2.61**	**0.12**	**3.80**	**0.19**
RC12–2 Phl	SEM	9	–	44.42	0.45	14.47	2.47	0.58	26.98	0.39	0.63	9.61
PHL–3 Phl[h]	**EMPA**	**8**	**0.9992**	**42.81**	**1.02**	**14.67**	**3.54**	**0.61**	**25.99**	**0.05**	**0.53**	**10.77**
RC12–2 Bt	SEM	16	–	39.29	1.11	9.82	25.97	0.00	13.35	0.00	0.96	9.45
Colorado Bt[e]	**WC**	**1**	**0.9779**	**40.60**	**4.43**	**13.59**	**18.66**	**0.14**	**13.22**	**1.70**	**0.73**	**6.79**
RC12–3												
RC12–3 Kln	TEM	16	–	53.41	0.34	45.13	1.07	0.06	0.00	0.00	0.00	0.00
Assam Kln[i]	**XRF**	**1**	**1.0000**	**53.12**	**0.67**	**45.03**	**1.18**	**0.00**	**0.00**	**0.00**	**0.00**	**0.00**
RC12–3 di-mica	TEM	1	–	56.86	0.00	13.14	11.67	0.00	0.00	5.27	1.39	11.67
Vesuvius Cel[j]	**WC**	**1**	**0.9877**	**59.40**	**0.00**	**11.71**	**11.27**	**0.00**	**7.05**	**0.32**	**0.11**	**10.02**
RC12–3 Ilt-Sme (70%–20%)	TEM	12	–	57.85	0.00	26.23	2.33	0.00	4.20	1.55	1.38	6.44
Woodbury Ilt-Sme (75%–25%)[k]	**XRF**	**1**	**0.9996**	**59.48**	**0.16**	**26.12**	**2.29**	**0.00**	**3.84**	**1.15**	**0.06**	**6.86**
RC12–3 Bt	SEM	27	–	42.09	1.68	11.51	20.40	0.93	14.14	0.22	0.00	8.87
Colorado Bt[f]	**WC**	**1**	**0.9946**	**40.60**	**4.43**	**13.59**	**18.66**	**0.14**	**13.22**	**1.70**	**0.73**	**6.79**
RC12–3 Chl (Mg)	SEM	8	–	39.83	0.00	21.84	0.00	0.00	38.0	0.12	0.00	0.21
Izu-Bonin Clc[l]	**EMPA**	**1**	**0.9936**	**39.69**	**0.00**	**25.66**	**0.98**	**0.15**	**33.1**	**0.19**	**0.13**	**0.09**
RC12–3 Chl (Fe)	TEM	27	–	27.61	0.00	20.02	43.43	0.15	7.95	0.44	0.00	0.00
Great Island Chm[m]	**WC**	**1**	**0.9918**	**30.55**	**0.39**	**19.63**	**38.19**	**0.00**	**6.84**	**0.25**	**0.51**	**0.14**

References: [a]Zhang *et al.* (2001), [b]Shimoda (1978), [c]Barrenechea *et al.* (2000), [d]Ross & Hendriks (1945), [e]Larsen *et al.* (1937), [f]Schwerdtner *et al.* (2007), [g]Warr *et al.* (2024), [h]Hillier *et al.* (2013; analysis included 0.55 wt.% P_2O_5), [i]Saikia *et al.* (2003), [j]Hendrick & Ross (1941), [k]Środoń *et al.* (1986), [l]Alt *et al.* (1998), [m]Battey (1956).
AAS = atomic absorption spectroscopy; WC = wet chemistry.
International Mineralogical Association (IMA)-approved mineral symbols and mixed-layer abbreviations (Warr, 2020, 2021): Bt = biotite; Cel = celadonite; Chl = chlorite; Chm = chamosite; Clc = clinochlore; Hly = halloysite; Ilt = illite; Kln = kaolinite; Mnt = montmorillonite; Ms = muscovite; Phl = phlogopite; Sme = smectite.

This dioctahedral structure is comparable to the montmorillonite in RC12-1, and its low layer charge closely matches that of the Wyoming montmorillonite from Upton Cross (Warr *et al.*, 2024), although the interlayer sites are enriched in Ca relative to Na.

The TEM-EDX analyses ($n = 23$) of the Fe-smectite contained an average of 17.04 wt.% Fe_2O_3 and is listed in the Reynolds Cup mixture as a nontronite (Table 2). However, this measured composition did not closely match the nontronites in the *MinMatch* database. The best match ($r = 0.9901$) ranked only 11th and exhibited a significantly lower SiO_2:Al_2O_3 ratio of 2.72 compared to the >4.3 ratios of the 10 nontronites in the database. The best overall fit ($r = 0.9958$) with a similar SiO_2:Al_2O_3 ratio of 3.71 was that of an Fe-rich montmorillonite from Woburn, UK, with the following dioctahedral structural formula:

$$(Si_{3.82}Al_{0.18})(Al_{1.03}Fe_{0.80}Mg_{0.16})(Ca_{0.13}Mg_{0.02}Na_{0.04}K_{0.01})O_{10}(OH_2)$$

This structure has a total layer charge of –0.37 (tetrahedral charge –0.18, octahedral charge –0.19) and is dominated by Ca- and Na-interlayer cations. As the Fe^{2+}/Fe^{3+} was not determined for this Fe-smectite, the structural formula should be considered an approximation, as it assumes that all Fe is Fe^{3+} and that there is no Fe substituting Si in the tetrahedral sites.

In addition to the two smectite minerals, the lower concentrations of kaolinite, di-mica, phlogopite and biotite were successfully identified in this mixture using both SEM and TEM. The di-mica (SEM-EDX, $n = 6$) corresponded closely with an illite $2M_1$ pattern from Athabasca (Zhang *et al.*, 2001), the phlogopite (SEM-EDX, $n = 9$) matched the PHL-3 composition of Hillier *et al.* (2013) and the biotite aligned with a sample composition reported by Larsen *et al.* (1937), despite the significantly greater Fe_2O_3 content of the EDX analyses. Although the biotite

https://doi.org/10.1180/clm.2026.10032 Published online by Cambridge University Press

Table 3. Comparison of powder compositions (main oxides, wt.%) based on XRF analyses, EDX compositions and XRD quantification (participant number 58) and mineral compositions given by *Profex* and XRD quantitation.

Oxide	XRF			EDX-based compositional mix			XRD-based compositional mix		
	RC12–1	RC12–2	RC12–3	RC12–1	RC12–2	RC12–3	RC12–1	RC12–2	RC12–3
SiO_2	55.58	63.78	72.98	55.24	62.78	72.98	57.87	64.53	67.83
TiO_2	3.69	0.30	2.40	3.61	0.54	2.40	2.41	0.15	1.85
Al_2O_3	27.12	18.64	7.74	28.22	17.98	7.74	29.45	21.01	9.62
Fe_2O_3	7.86	8.64	5.44	7.35	8.66	5.44	3.28	6.00	6.40
MnO_2	0.11	0.03	0.18	0.04	0.14	0.15	0.05	0.18	0.09
MgO	0.76	2.38	1.89	0.81	3.31	1.89	0.72	2.40	2.71
CaO	2.52	2.00	5.44	1.35	2.13	5.44	1.33	2.31	5.38
Na_2O	0.35	2.68	1.47	0.00	2.06	1.46	0.10	1.14	1.51
K_2O	1.10	1.01	1.30	1.10	2.33	1.33	0.83	1.13	1.05
P_2O_5	0.91	0.49	0.04	0.88	0.00	0.00	0.82	0.41	0.00
BaO	0.01	0.02	0.57	0.01	0.02	0.57	0.01	0.02	0.41
ZrO	0.01	0.02	0.55	0.00	0.01	0.55	0.00	0.02	0.63
Sum	100	100	100	100	100	100.3	100	100	100
Mean % difference	–	–	–	0.29	0.63	0.04	1.00	1.04	0.79

reference composition was derived using wet chemical methods rather than modern microprobe analyses, this exceptionally pure iron-rich biotite has provided a reliable benchmark for constraining the annite-phlogopite series (Rieder *et al.*, 1998). This slightly lower match ($r = 0.9779$) probably reflects the limited number of biotite compositions currently included in the database ($n = 5$), which reduces the ability to fully capture the compositional diversity of this mineral.

RC12-3

MinMatch analysis of RC12-3 clay mineral compositions confirmed the presence of a mixture of kaolinite, mica, illite-smectite, biotite and two types of chlorites: clinochlore and chamosite (Tables 1 & 2). The kaolinite composition closely matched that of Assam, India (Saikia *et al.*, 2003), although it exhibited slight differences from RC12-1 and RC12-2, particularly in the trace concentrations of Ti, Fe, Mn, Mg, Ca and Na. These minor variations are probably due to the presence of very fine accessory minerals rather than reflecting true compositional differences in the kaolinite itself.

The di-mica component was best matched to a celadonite composition from Vesuvius; however, this identification was based on a single TEM-EDX analysis and should therefore be considered tentative. By contrast, the illite-smectite component produced a more robust result. Twelve particle analyses indicated that an illite-smectite structure (75%-25%) from Woodbury, UK (Środoń *et al.*, 1986), most closely matched the illite-smectite composition (70%-30%) determined by XRD (value provided by S. Hillier). The procedure used to establish this match is illustrated in Fig. 4, which presents both the Pearson correlation coefficient (r) and the SiO_2:Al_2O_3 ratios for the top 25 candidate illite-smectite structures, including the end-members illite and smectite. The trend in the dataset was approximated by fitting a third-order polynomial curve ($R^2 = 0.42$), reflecting a moderate correlation between r and the illite content (%) in illite-smectite minerals (Fig. 4a). The highest r value of 0.9996 corresponds closely to the main peak, reflecting a high illite content in the illite-smectite mineral. Considering the standard deviation (±1σ of 0.0002, $n = 12$), all matched samples within the range 0.9994–0.9998 are regarded as statistically indistinguishable and thus represent plausible solutions. These correspond to illite-smectite compositions with ~60–80% illite-layer abundance.

As a secondary criterion, the measured SiO_2:Al_2O_3 ratios of the top 25 matches (ranked by r) were examined (Fig. 4b). Although no significant correlation is observed between the SiO_2:Al_2O_3 ratio and illite content ($R^2 = 0.08$), the measured value of 2.21 compares reasonably well with the 2.28 ratio of the Woodbury illite-smectite composition (Środoń *et al.*, 1986), consistent with the general pattern observed for all oxide concentrations (Fig. 2). Considering analytical uncertainty (±1σ of 0.06, $n = 12$), the more reliable SiO_2:Al_2O_3 ratios are estimated to lie within the range 2.15–2.27.

Based on the average TEM-EDX analyses of the illite-smectite of the RC12-3 sample, structural formulas for this mineral and for the Woodbury illite-smectite can be written as follows:

$$\text{illite-smectite} = (Si_{3.57}Al_{0.43})(Al_{1.48}Fe_{0.11}Mg_{0.43})(Ca_{0.10}Na_{0.17}K_{0.51})O_{10}(OH_2)$$

$$\text{Woodbury illite-smectite} = (Si_{3.65}Al_{0.35})(Al_{1.54}Fe_{0.11}Mg_{0.35})(Ca_{0.08}Na_{0.01}K_{0.54})O_{10}(OH_2)$$

with calculated total layer charges of –0.80 and –0.70 per $O_{10}(OH)_2$, respectively.

Similarly, the TEM and SEM-EDX compositions of the biotite ($n = 27$), clinochlore ($n = 8$) and chamosite ($n = 27$) particles could be successfully matched to reference compositions in the database. Although the biotite composition did not allow for a reliable structural formula, the two chlorite compositions yielded approximate stoichiometric formulas as follows:

$$\text{clinochlore} = (Mg_{4.53}Al_{1.25})_{5.87}(Si_{3.19}Al_{0.81})_{4.00}O_{10}(OH)_8$$

$$\text{chamosite} = (Fe^{2+}{}_{3.38}Mg_{1.23}Al_{1.30}Mn_{0.01})_{5.92}(Si_{2.86}Al_{1.14})_{4.00}O_{10}(OH)_8$$

The clinochlore composition with the highest correlation ($r = 0.99$) corresponded to a forearc Izu–Bonin sample from Ocean Drilling Program (ODP) Hole 786B (Alt *et al.*, 1998), whereas the best-fitting chamosite (also $r = 0.99$) matched a specimen from the Great Island spilite, New Zealand (Table 2; Battey, 1956).

https://doi.org/10.1180/clm.2026.10032 Published online by Cambridge University Press

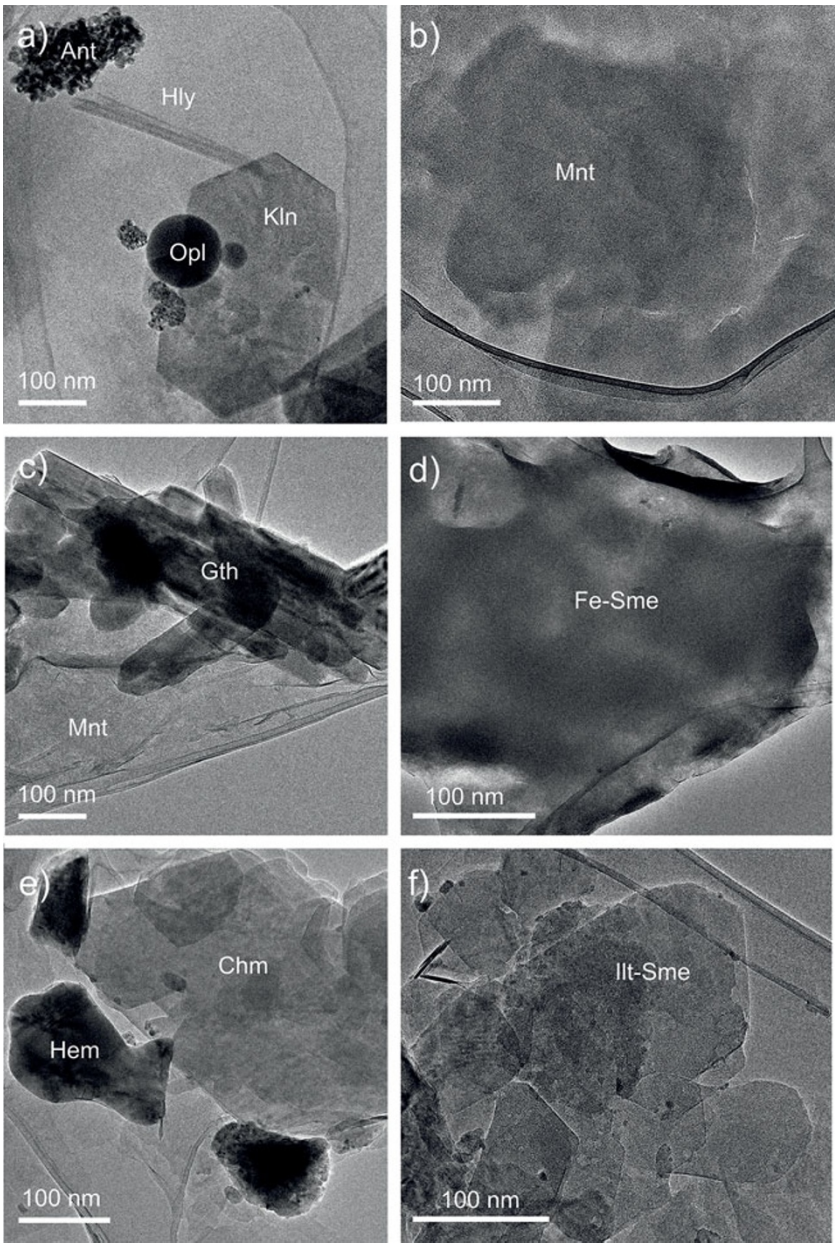


Figure 3. TEM images of <2 μm-sized minerals: (a,b) RC12-1, (c,d) RC12-2 and (e,f) RC12-3. Ant = anatase; Chm = chamosite; Fe-Sme = Fe-smectite; Gth = goethite; Hem = hematite; Hly = halloysite; Ilt-Sme = illite-smectite; Kln = kaolinite; Mnt = montmorillonite (International Mineralogical Association (IMA) symbols from Warr, 2020, 2021).

Composition analyses of accessory phases

Secondary electron imaging of multiple regions within the >2 μm size fractions revealed well-isolated grains suitable for high-quality EDX mapping (Figs 5 & S1). These regions were selected based on their relatively uniform mineral distribution and minimal particle aggregation. Mineral identification was performed using the *MinMatch* program, utilizing multiple-area EDX analyses of individual grains, and the results are summarized on the corresponding SEM images (Fig. 5).

Several limitations inherent to EDX analyses affected the performance of *MinMatch* in identifying accessory mineral phases. The inability to detect hydrogen prevented differentiation between oxides and hydroxides, and the presence of the substrate film hindered reliable quantification of carbon. Additionally, the Fe^{2+}/Fe^{3+} ratio could not be determined, which restricted the interpretation of iron-bearing minerals. The mineral database is primarily optimized for aluminosilicate minerals, which reduces its effectiveness for other mineral groups such as phosphates, sulfates, sulfides and carbonates. Despite these limitations, reliable element maps could be routinely obtained for Si, Ti, Al, Fe, Mg. Ca, Na, K, P, Ba and S (Fig. S1). The distribution of Zr-*K*α (2.04 keV) could also be mapped; however, this peak overlaps with P-*K*α (2.01 keV), introducing uncertainty when trying to distinguish between these two elements using EDX.

MinMatch also failed to identify a number of minerals present at very low or trace concentrations (<0.2 wt.%), such as amphibole, corundum, ilmenite and talc, which occurred in the RC12-2 and RC12-3 mixtures.

https://doi.org/10.1180/clm.2026.10032 Published online by Cambridge University Press

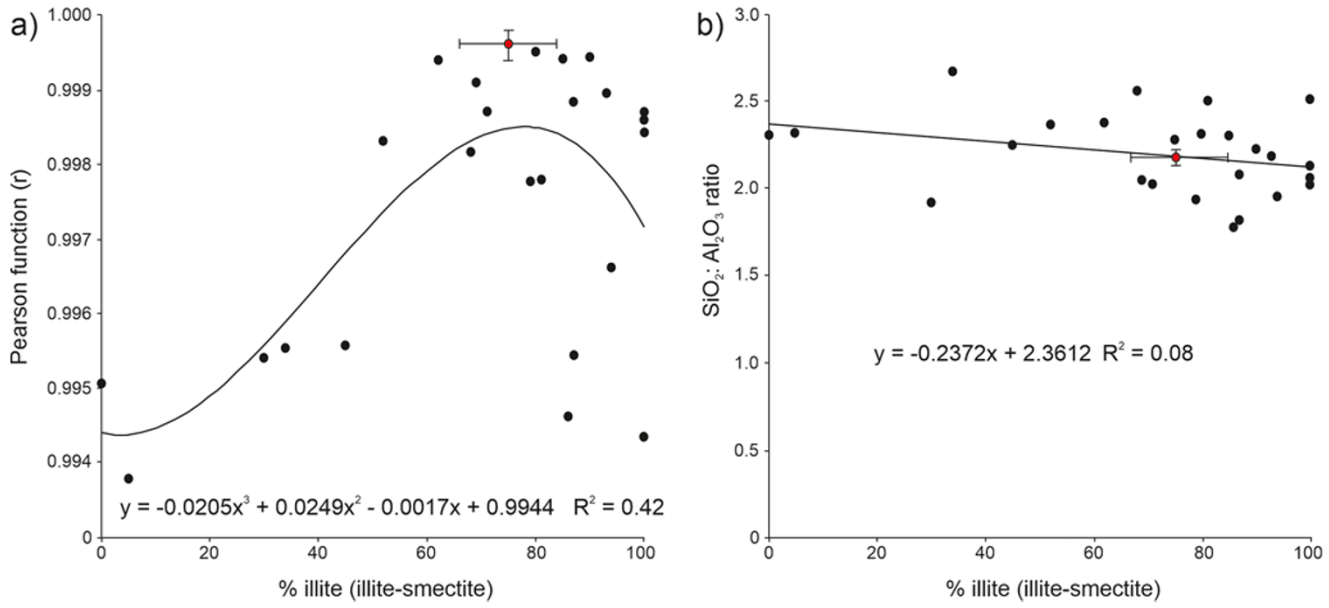


Figure 4. (a) Top 25 Pearson function mineral fits (r) to the mixed-layered illite-smectite mineral in the RC12-3 sample. The observed data are approximated using a third-order polynomial curve. The best-fit (highest r) value of 0.9997 reflects an Reichweite 1 (R1; short-range ordering) illite-smectite (75%-25%) composition from the database. (b) The SiO_2:Al_2O_3 ratios for the top 25 matches obtained for the same dataset as (a). The raw data have a SiO_2:Al_2O_3 ratio of 2.21, marked on the graph as a red data point. Error bars represent the calculated standard deviation (±1σ, n = 12).

Feldspar compositions

One group of minerals for which *MinMatch* performed particularly well was the feldspars, whose precise identification and quantification using XRD remain challenging. For example, RC12-3 contained three feldspar species – microcline, albite and a plagioclase (labradorite) – all of which were successfully identified using *MinMatch* (Fig. 6). The microcline was best matched with a composition from Nora Kärr, Sweden (MacKenzie, 1954), yielding $r = 0.9997$, and its SiO_2:Al_2O_3 ratio of 3.47 compared reasonably well with the measured value of 3.74. The best-fitting albite was that reported by Kracek & Neuvonen (1952) from Virginia, USA, with $r = 0.9998$ and a closely matching SiO_2:Al_2O_3 ratio (3.45 compared with the measured value of 3.53). A second albite match from Val Devero, Italy (Azzini, 1933), also yielded $r = 0.9996$, with a slightly lower SiO_2:Al_2O_3 ratio of 3.29. For the plagioclase (labradorite), the best fit was an andesine feldspar from Madras, India (Howie, 1955), with $r = 0.9995$, which most accurately reproduced the average Ca and Na contents measured by SEM-EDX (n = 8). Its SiO_2:Al_2O_3 ratio of 2.20 matched well with the measured ratio of 2.13. The second-best fit was a labradorite feldspar from Utah, USA (Meen, 1933), with $r = 0.9946$; however, this composition exhibited a significantly lower SiO_2:Al_2O_3 ratio (1.78) than the measured ratio.

Oxides, hydroxides, oxyhydroxides and carbonates

Despite the challenges in differentiating Fe oxide and oxyhydroxide minerals, such as goethite, hematite and magnetite, whose EDX compositions are effectively indistinguishable, additional diagnostic information was obtained from their characteristic crystal morphologies. For example, goethite (2.2 wt.%), in RC12-1 was positively identified based on its flat, lath-shaped crystals (Fig. 3). In contrast, goethite was not detected in RC12-2, despite being present at a similar abundance (2.2 wt.%). Hematite and magnetite in RC12-2 could not be discriminated using EDX compositions alone; their presence was instead inferred from supplementary observations, including the magnetic behaviour of small black grains in RC12-2 and the intense red colouration associated with hematite in RC12-3.

Similarly, the distinct crystal morphologies of TiO_2 grains allowed anatase and rutile to be distinguished in RC12-1. In contrast, only rutile crystals were detected in RC12-3, whereas anatase, present at 0.1 wt.%, was not detected. Additionally, the 3.4 wt.% cristobalite present in RC12-2 could not be reliably distinguished from quartz.

Amorphous phases

The amorphous SiO_2 phase (opal) in RC12-1 was successfully identified based on the spherical grain morphology (Fig. 3a) and the absence of electron diffraction patterns during selective-area TEM analyses. In contrast, the amorphous obsidian glass in RC12-2 was not recognized, primarily because glass compositions were not included in the *MinMatch* database at the time. Since then, eight glass compositions, ranging from obsidian to basaltic glasses, have been added to the database. Re-evaluation of some compositions previously attributed to sanidine feldspars indicated a closer match to obsidian glass; however, characteristic grain shapes for glass were not recognized, and these grains could not be reliably distinguished from feldspars.

Non-oxide minerals

The carbonate polymorphs calcite and aragonite could not be reliably distinguished. Dolomite, however, was recognized in RC12-3 based on its Mg-Ca composition. Apatite was identified in two samples on the basis of its Ca-phosphate chemistry, while pyrite was recognized in RC12-1 based on its Fe-S composition. Baryte was also identified in RC12-3.

https://doi.org/10.1180/clm.2026.10032 Published online by Cambridge University Press

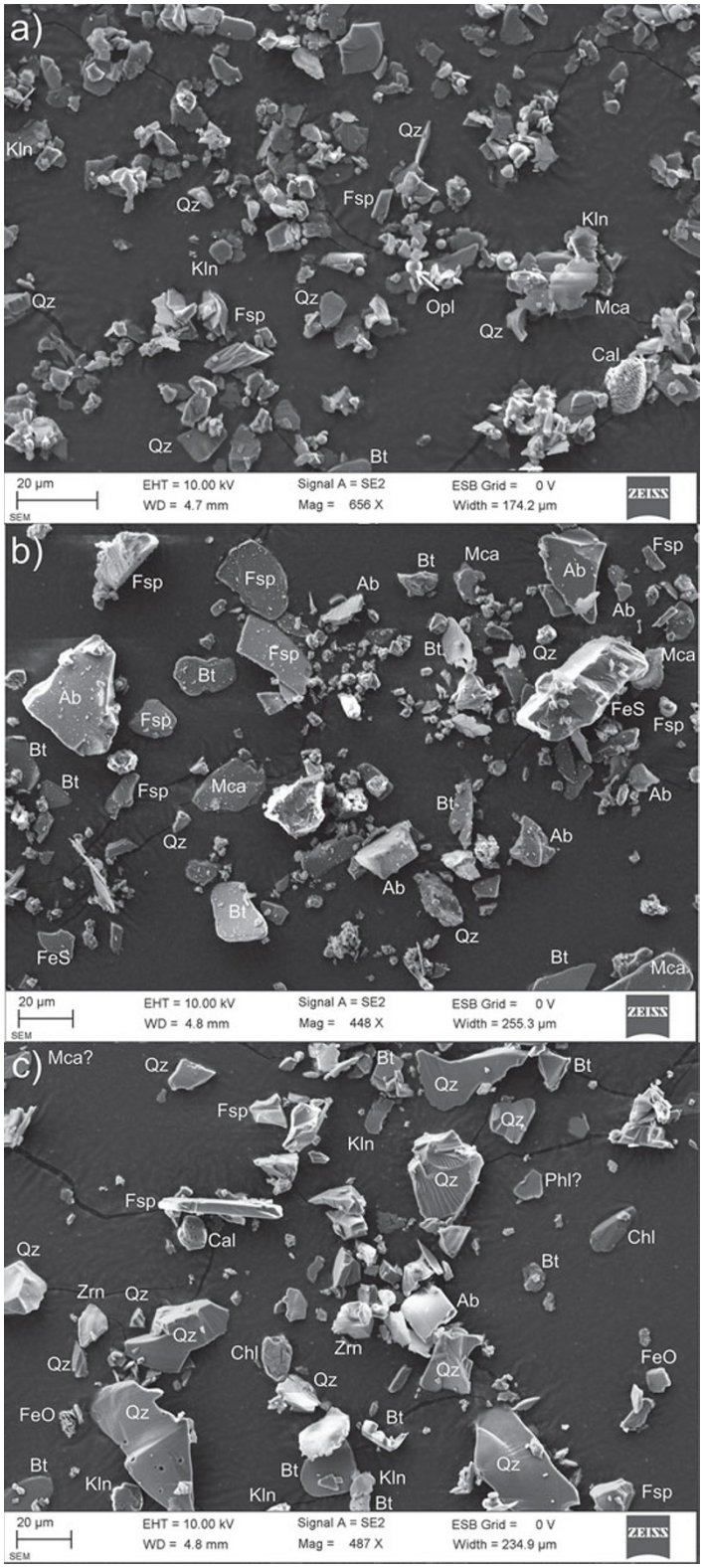


Figure 5. SEM secondary electron images of the coarse fractions (>2 µm): (a) RC12-1, (b) RC12-2 and (c) RC12-3. International Mineralogical Association (IMA)-approved mineral symbols after Warr (2021): Ab = albite; Bt = biotite; Cal = calcite; Fsp = feldspar; Kln = kaolinite; Mca = mica; Opl = opal; Qz = quartz.

Compositional mass balancing and combining with XRD Rietveld quantifications

Rietveld refinement programs, such as *Profex* (Doebelin & Kleeberg, 2015), provide the summed oxide composition derived from the mineral structure files, enabling direct comparison with the bulk powder composition obtained by XRF. This comparison can be used to refine overall quantifications through mass-balancing procedures (Rahfeld *et al.*, 2018). For the XRD quantifications conducted in this study (participant 58), the summed oxide totals differed from the XRF bulk compositions by 1.00, 1.04 and

https://doi.org/10.1180/clm.2026.10032 Published online by Cambridge University Press

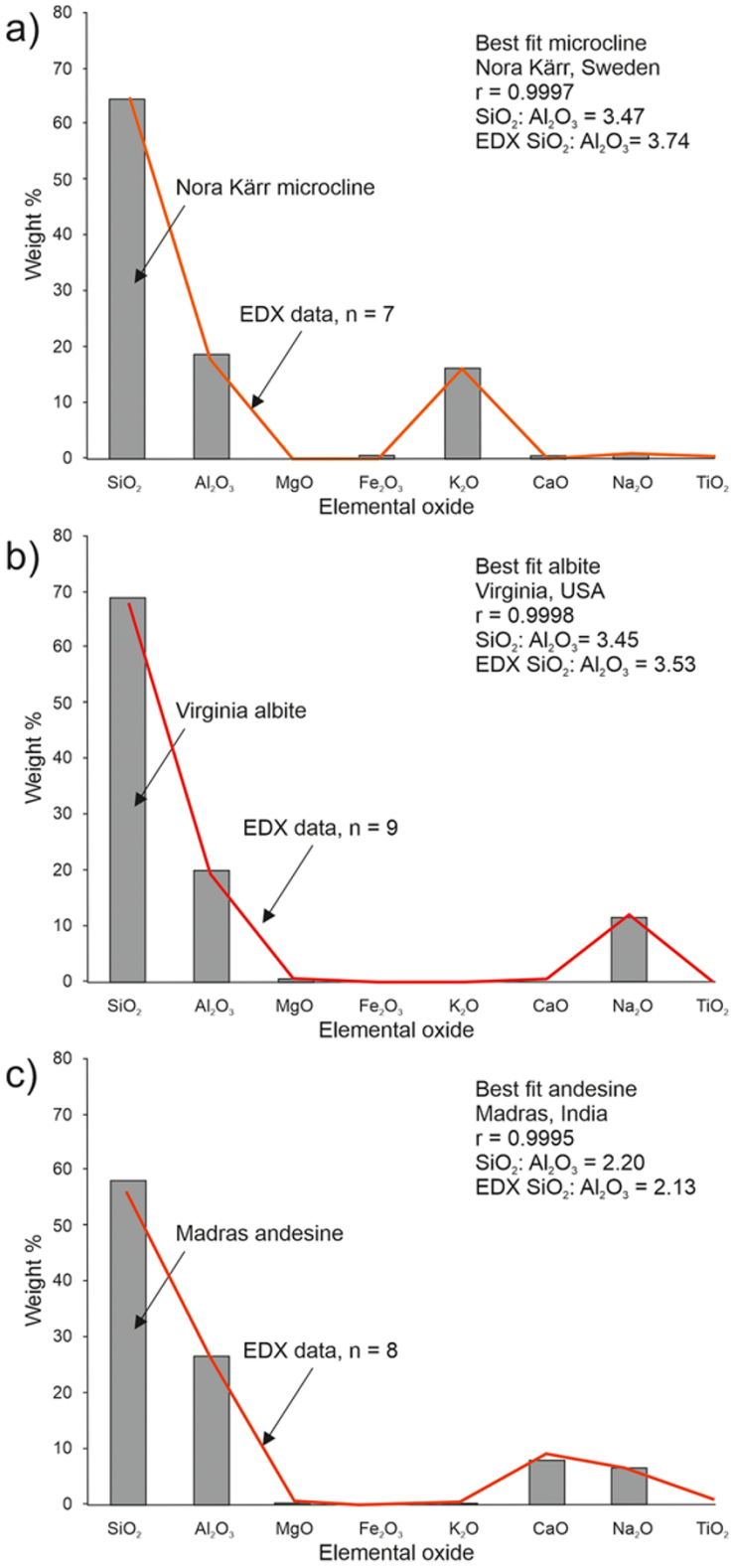


Figure 6. *MinMatch*'s best-fit composition for the three felspars present in RC12-3. (a) Microcline fit to the SEM-EDX data from Nora Kärr, Sweden (MacKenzie, 1954). (b) Albite fit to the SEM-EDX data from Virginia, USA (Kracek & Neuvonen, 1952). (c) Andesine fit to the plagioclase (described as labradorite) to the SEM-EDX data from Madras, India (Meen, 1933).

0.79 wt.% oxides for the RC12-1, RC12-2 and RC12-3 mixtures, respectively (see Supplementary Material).

As a comparison, the EDX-based compositional analyses of both clay minerals and the accessory phases were used to refine the XRD-based quantification results through a stepwise procedure. First, a list of minerals considered present was compiled based on combined XRD and SEM/TEM-EDX results, with *Profex*-derived values serving as the initial estimates of mineral abundances. Oxide concentrations were then manually adjusted by identifying the mineral(s) contributing the dominant proportion of each element and iteratively modifying their abundances to achieve best agreement with the corresponding bulk XRF concentration.

https://doi.org/10.1180/clm.2026.10032 Published online by Cambridge University Press

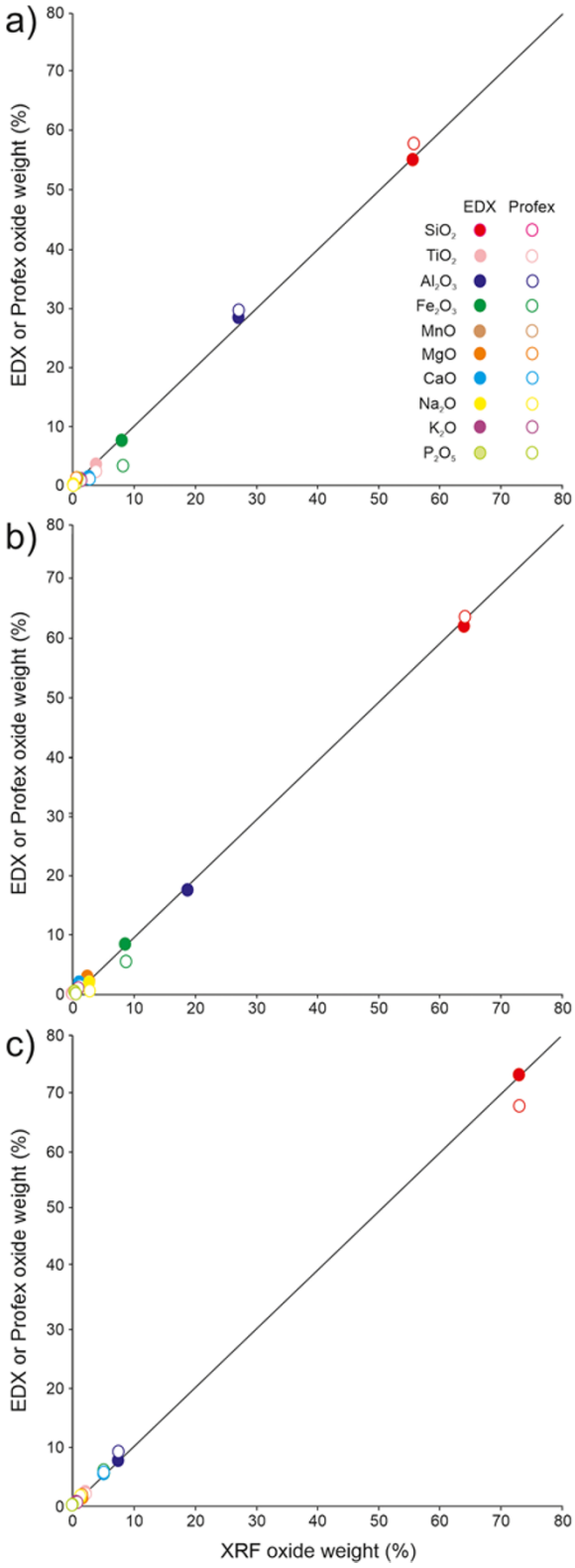


Figure 7. Bulk oxide weight (%) results plot for (a) RC12-1, (b) RC12-2 and (c) RC12-3, showing the mass-balanced results using the EDX-derived compositions (solid circles) and XRD quantifications of the mineral components, as well as those given by *Profex* (open circles). The average differences between the datasets are given in Table 3. The diagonal lines represent 1:1 relationships.

For example, in sample RC12-2, the principal contributors were quartz and heulandite for SiO_2, muscovite and kaolinite for Al_2O_3, muscovite and phlogopite for K_2O and plagioclase, dolomite and fluorapatite for CaO. These adjustments were made in a spreadsheet to minimize differences between the EDX-derived elemental mixtures and the bulk XRF data. Finally, the abundances

https://doi.org/10.1180/clm.2026.10032 Published online by Cambridge University Press

of the remaining minerals were also optimized to further improve the overall agreement between calculated and measured oxide compositions.

This procedure was applied to all three RC12 samples, and the manually mass-balanced, EDX-derived oxide wt.% values were compared with the XRF-derived abundances and the XRD-derived compositions obtained using *Profex* (Fig. 7). Improvements in compositional matching were observed across all three samples, with all final mass-balanced adjustments showing mean differences of less than 0.5 wt.% oxides relative to the bulk chemistry for each sample. Although mathematically optimized, these adjustments did not result in improved overall quantification. This outcome is attributed to the *MinMatch* programme failing to identify several accessory minerals, which consequently distorted the calculated values.

Furthermore, multiple valid approaches probably exist for balancing the compositions, as several minerals exhibit similar elemental signatures. Consequently, there are multiple solutions that can minimize the differences between the chemical mixture model and the XRF results. Mass-balance procedures can also be attempted, such as non-negative least square regression analyses, although the outcomes may vary considerably depending on the assumptions employed.

A more realistic approach would be to integrate EDX-derived oxide chemistries directly into Rietveld refinement workflows, allowing mineral compositions obtained from EDX to dynamically update structural parameters such as site occupancies and formula weights, effectively serving as a quantitative calibration library. This integration could improve the non-unique best-fit mineral structures selected from refinement libraries, as chemically constrained models yield more realistic stoichiometric structures. It would also enhance the identification of intermediate phases within solid-solution series, such as albite-anorthite feldspars and chamosite-clinochlore chlorites. With expanded reference databases and more robust accessory mineral detection, this combined approach could ultimately become a standard procedure for achieving internally consistent and reproducible mineralogical quantifications.

Summary and conclusions

The *MinMatch.xls* program is a robust, reference-based tool for the rapid, reliable identification of clay minerals and accessory phases using measured oxide compositions. It compares measured data with over 500 reference datasets. Potential matches are ranked using the Pearson correlation coefficient (r), along with secondary criteria, including the SiO_2:Al_2O_3 ratio, other statistical parameters and visual inspection of graphical patterns. This approach provides objective and reproducible results for fine-grained materials.

Application to the 12th Reynolds Cup samples demonstrated accurate identification of clay minerals, coarser phyllosilicates, feldspars and other accessory components. Fine-grained fractions (<1–2 μm) were characterized by TEM-EDX and coarser grains by SEM-EDX. Best-fit compositions had high correlations ($r > 0.9779$), confirming the program's precision. Closely related minerals, including illite-smectites, dioctahedral smectites and chlorite species, were reliably distinguished. Feldspars and carbonates were also accurately identified, although differentiation of iron oxides and oxyhydroxides remained limited.

Integration with mass-balance and XRD analyses improved agreement with bulk XRF data (mean differences <0.5 wt.% oxides), supporting quantitative workflows. Although some trace accessory minerals were not detected, the method provides a strong basis for combining chemical, structural and morphological data to achieve comprehensive sample characterisation.

MinMatch offers an efficient and accurate approach for identifying clay minerals and associated phases and is complementary to other analytical techniques. Future improvements, including expanded reference databases, enhanced detection of accessory phases and integration with iterative Rietveld refinement workflows, could further increase its capability to resolve complex, fine-grained assemblages.

Supplementary material. The supplementary material for this article can be found at https://doi.org/10.1180/clm.2026.10032. The latest version of *MinMatch* is available from the corresponding author upon request.

Acknowledgements. We thank the teachers and participants of past DTTG workshops, where this *MinMatch* program has been presented, tested and refined. We also thank Steve Hillier for providing the necessary information concerning the 12th Reynolds Cup samples. The manuscript text was improved based on language suggestions from Grammarly and ChatGPT-5. The authors thank Duncan Pirrie and an anonymous reviewer for their constructive comments on the submitted version of the manuscript.

Financial support. The JEOL 2100 Plus TEM microscope used in this study was financed by the Deutsche Forschungsgemeinschaft (DFG project number 428027021; https://gepris.dfg.de/gepris/projekt/428027021).

Competing interests. The authors declare none.

References

Alt J.C., Teagle D.A.H., Brewer T., Shanks W.C. III & Halliday A. (1998) Alteration and mineralization of an oceanic forearc and the ophiolite-ocean crust analogy. *Journal of Geophysical Research*, **103**, 12365–12380.

Azzini F. (1933) Adularia e albite di Val Devero (Ossola). *Atti dell'Accademia di Scienze, Lettere ed Arti di Venezia-Trentino-Istriana*, **46**, 65–80.

Barrenechea J.F., Rodas M., Frey M., Alonso-Azcárate J. & Mas J.R. (2000) Chlorite, corrensite, and chlorite-mica in Late Jurassic fluvio-lacustrine sediments of the Cameros Basin of northeastern Spain. *Clays and Clay Minerals*, **48**, 256–265.

Battey M.H. (1956) The petrogenesis of a spilitic rock series from New Zealand. *Geological Magazine*, **93**, 89–110.

Bergaya F. & Lagaly G. (editors) (2013) *Handbook of Clay Science*, 2nd edition. Elsevier, Amsterdam, The Netherlands, 1420 pp.

Biswas B., Warr L.N. & Saha B. (2023) Understanding iron impurities in Australian kaolin and their effect on acid and heat activation processes of clay. *ACS Omega*, **8**, 5533–5544.

Biswas B., Grathoff G., Naidu R. & Warr L. N. (2024) The multidisciplinary science of applied clay research: a 2021–2023 bibliographic analysis. *Applied Clay Science*, **258**, 107471.

Boraiy M., El-Metwally M., Borbon A. & Chevailler (2024) Elemental ratios as tracers of the sources of mineral dust in north-eastern Sahara. *International Journal of Environmental Science and Technology*, **21**, 1875–1888.

Brigatti M.F. (2018) Relationships between composition and structure in Fe-rich smectites. *Clay Minerals*, **18**, 177–186.

Brindley G.W. & Brown G. (editors) (1984) *Crystal Structures of Clay Minerals and Their X-Ray Identification*, 2nd edition. Mineralogical Society, London, UK, 544 pp.

Christidis G.E., Chryssikos G.D., Derkowski A., Dohrmann R., Eberl D.D., Joussein E. & Kaufhold S. (2023) Methods for determination of the layer charge of smectites: a critical assessment of existing approaches. *Clays and Clay Minerals*, **71**, 25–53.

Deer W.A., Howie R.A. & Zussman J. (1992) *An Introduction to the Rock-Forming* Minerals, 2nd edition. Longman, London, UK, 696 pp.

Deer W.A., Howie R.A. & Zussman J. (2013) *An Introduction to the Rock-Forming Minerals*, 3rd edition. Longman, London, UK, 498 pp.

Doebelin N. & Kleeberg R. (2015) *Profex*: a graphical user interface for the Rietveld refinement program *BGMN*. *Journal of Applied Crystallography*, **48**, 1573–1580.

Droop G.T.R. (1987) A general equation for estimating Fe^{3+} concentrations in ferromagnesian silicates by microprobe analysis using stoichiometric criteria. *Mineralogical Magazine*, **51**, 431–435.

Fandrich R., Gu Y., Burrows D. & Moeller K. (2007) Modern SEM-based mineral liberation analysis. *International Journal of Mineral Processing*, **84**, 310–320.

Fawcett T.G., Blanton J.R., Kabekkodu S.N. & Blanton T.N. (2018) Mineral identification by elemental composition: a new tool within PDF-4 databases. *Powder Diffraction*, **33**, 156–161.

Fleet M.E. (2003) *Rock-Forming Minerals. Volume 3A: Sheet Silicates: Micas*, 2nd edition (W.A. Deer, R.A. Howie, J. Zussman, editors). Geological Society of London, London, UK, 758 pp.

Garcia-Romero E., Lorenzo A., García-Vicente A., Morales J., García-Rivas, J. & Suárez, M. (2021) On the structural formula of smectites: a review and new data on the influence of exchangeable cations. *Journal of Applied Crystallography*, **54**, 251–262.

Gottlieb P., Wilkie G., Sutherland D., Ho-Tun E., Suthers S., Perera K. *et al.* (2000) Using quantitative electron microscopy for process mineralogy applications. *JOM*, **52**, 24–25.

Gum Y. (2003) Automated scanning electron microscope based mineral liberation analysis. An Introduction to JKMRC/FEI mineral liberation analyser. *Journal of Minerals & Materials Characterization & Engineering*, **2**, 33–41.

Han S., Löhr S.C., Abbott A.N., Baldermann A., Farkaš J., McMahon W. *et al.* (2022) Earth system science applications of next-generation SEM-EDS automated mineral mapping. *Frontiers in Earth Science*, **10**, 956912.

Hendrick S.B. & Ross C.S. (1941) Chemical composition and genesis of glauconite and celadonite. *American Mineralogist*, **26**, 683–708.

Hillier S., Marwa E.M.M. & Rice C.M. (2013) On the mechanism of exfoliation of 'vermiculite'. *Clay Minerals*, **48**, 563–582.

Howie R.A. (1955) The geochemistry of the charnockite series of Madras, India. *Earth and Environmental Science Transactions of the Royal Society of Edinburgh*, **62**, 725–768.

Kracek F.C. & Neuvonen K.J. (1952) Thermochemistry of plagioclase and alkali feldspars. *American Journal of Science*, **A250**, 293–317.

Larsen E.S., Irving J., Gonyer F.A. & Larsen E.S. III (1937) Petrologic results of a study of the minerals from the Tertiary volcanic rocks of the San Juan region, Colorado. Pt. 5, the amphiboles; Pt. 6, biotite. *American Mineralogist*, **22**, 889–905.

MacKenzie W.M. (1954) The orthoclase-microcline inversion. *Mineralogical magazine and Journal of the Mineralogical Society*, **30**, 354–366.

Madejová J. (2003) FTIR techniques in clay mineral studies. *Vibrational Spectroscopy*, **31**, 1–10.

Meen V.B. (1933) A description of a few plagioclases. *University of Toronto Studies. Geological Series*, **35**, 47–50.

Moore D M. & Reynolds R.C. Jr (1997) *X-Ray Diffraction and the Identification and Analysis of Clay Minerals*, 2nd edition. Oxford University Press, New York, NY, USA, 400 pp.

Newman A.C.D. & Brown G. (1987) The chemical constitution of clays. Pp. 1–128 in: *Chemistry of Clays and Clay Minerals* (A.C.D. Newman, editor). Monograph 6. Mineralogical Society, London, UK.

Pirrie D., Rollinson G.K., Power M.R. & Webb J. (2013) Automated forensic soil mineral analysis; testing the potential of lithotyping. *Geological Society, London, Special Publications*, **384**, 47–64.

Podlech C., Matschiavelli N., Peltz M., Kluge S., Arnold T., Cherkouk A. *et al.* (2021) Bentonite alteration in batch reactor experiments with and without organic supplements: implications for the disposal of radioactive waste. *Minerals*, **11**, 932.

Rahfeld A., Kleeberg R., Möckel R. & Gutzmer, J. (2018) Quantitative mineralogical analysis of European Kupferschiefer ore. *Mineral Engineering*, **115**, 21–32.

Rieder M., Cavazzini G. D'yakonov Y.S., Frank-Kamenetskii V.A., Gottardi G., Guggenheim S. *et al.* (1998) Nomenclature of the micas. *Clays and Clay Minerals*, **46**, 586–595.

Ross C.S. & Hendricks S. B. (1945) *Minerals of the Montmorillonite Group: Their Origin and Relation to Soils and Clays*. US Government Printing Office, Washington, DC, USA, 79 pp.

Saikia N.J. Bharali D.J., Sengupta P., Bordoloi D., Goswamee R.L., Saikia P.C. & Borthakur P.C. (2003) Characterization, beneficiation and utilization of a kaolinite clay from Assam, India. *Applied Clay Science*, **24**, 93–103.

Schwerdtner G., Anger H. & Störr M. (2007) *Die Kaolinlagerstätten des Kemmlitzer Reviers*. Bergbaumonographie, Freiberg, Germany, 116 pp.

Shimoda S. (1978) Interstratified minerals. *Developments in Sedimentology*, **26**, 265–322.

Siebach K.L., Moreland E.L., Costin G. & Jiang Y. (2026) *MIST*: an online tool automating mineral identification by stoichiometry. *Computers & Geosciences*, **206**, 106021.

Środoń J. (2006) Identification and quantitative analysis of clay minerals. Pp. 765–787 in: *Handbook of Clay Science*, Vol. 1 (F. Bergaya, B.K.G. Theng & G. Lagaly, editors), Elsevier, Amsterdam, The Netherlands.

Środoń J., Morgan D.J. & Eslinger E.V. (1986) Chemistry of illite/smectite and end-member illite. *Clays and Clay Minerals*, **34**, 368–378.

Stanley C.R. (2020) Molar element ratio analysis of lithogeochemical data: a toolbox for use in mineral exploration and mining. *Geochemistry: Exploration, Environment, Analysis*, **20**, 233–256.

Sudheer Kumar, R., Warr L.N., Thombare B.R., Manzel T. & Grathoff G.H. (2026). Hematite neocrystallisation derived from the experimental alteration of montmorillonite in NaCl solution. *Applied Clay Science*, **279**, 108008.

Vali H., Martin R.F., Amarantidis G. & Morteani G. (1993) Smectite-group minerals in deep-sea sediments: monomineralic solid-solutions or multiphase mixtures? *American Mineralogist*, **78**, 1217–1229.

Warr L.N. (2020) Recommended abbreviations for the names of clay minerals and associated phases. *Clay Minerals*, **55**, 261–264.

Warr L.N. (2021) IMA–CNMNC approved mineral symbols. *Mineralogical Magazine*, **85**, 291–320.

Warr L.N., Thombare B.R., Kumar R.S., Peltz M. & Grathoff G.H. (2024) Determining the stoichiometric composition of Wyoming montmorillonite using improved transmission electron microscopy energy dispersive X-ray (TEM-EDX) techniques. *Clays and Clay Minerals*, **72**, 1–20.

Wilson M.J. (2013) *Rock-Forming Minerals. Volume 3C: Sheet Silicates: Clay Minerals*, 2nd edition (A. Deer, R.A. Howie & J. Zussman, editors). Geological Society of London, London, UK, 736 pp.

Xia M., Liu H., Wang H., Sun F., Zou X., Chen T. *et al.* (2021) Impact of the interaction between hematite and halloysite on environmental fate of organic pollutants. *Applied Clay Science*, **209**, 106123.

Yavuz F. (2003) Evaluating micas in petrologic and metallogenic aspect: I – definitions and structure of the computer program *MICA*. *Computers & Geosciences*, **29**, 1203–1213.

Yavuz F., Kumral M., Karakaya N., Karakaya M.T. & Yildirim D.K. (2015) A *Windows* program for chlorite calculation and classification. *Computers & Geosciences*, **81**, 101–113.

Zhang G., Wasyluik K. & Pan, Y. (2001) The characterization and quantitative analysis of clay minerals in the Athabasca Basin, Saskatchewan: application of shortwave infrared reflectance spectroscopy. *The Canadian Mineralogist*, **39**, 1347–1363.

https://doi.org/10.1180/clm.2026.10032 Published online by Cambridge University Press